applied sciences

MDPI

Article

Numerical Evaluation of the Equivalent Damping Ratio Due to Dissipative Roof Structure in the Retrofit of Historical Churches

Nicola Longarini [1,*], Pietro Crespi [1], Marco Zucca [2] and Manuela Scamardo [1]

[1] Architecture, Built Environment and Construction Engineering Department, Politecnico di Milano, Piazza Leonardo da Vinci 32, 20133 Milan, Italy; pietro.crespi@polimi.it (P.C.); manuela.scamardo@polimi.it (M.S.)
[2] Department of Civil Environmental Engineering and Architecture, University of Cagliari, Via Marengo 2, 09123 Cagliari, Italy; marco.zucca2@unica.it
[*] Correspondence: nicola.longarini@polimi.it

Abstract: This paper is focused on the numerical evaluation of the equivalent damping ratio (EDR) given by a dissipative wood-based roof diaphragm in the seismic retrofitting of single-nave historical churches. In the design phase, the EDR could be a key parameter to select the optimal roof structure configuration, thereby obtaining the maximum energy dissipation. In this way, the roof structure works as a damper to facilitate a box behavior of the structure during the seismic response. The EDR measures the energy dissipated by the nonlinear behavior of the roof's steel connections and masonry walls during seismic events. In a preliminary retrofitting design phase, an initial implementation of the geometries of the walls and the chosen geometry for the roof is carried out by adopting an equivalent frame model (FEM) with inelastic rotational hinges for the nonlinear properties of the masonry walls and inelastic shear hinges for the nonlinear behavior of the roof's steel connections. Since, for historical churches, the transversal response under seismic events is the worst situation for the single-nave configuration, the earthquake is applied as transversal accelerograms. In this way, the damped rocking of the perimeter walls due to the dissipative roof diaphragm can be described in terms of a hysteretic variable. By varying the value of the hysteretic variable, possible configurations of the roof diaphragm are tested in the design phase, considering the different shear deformation values of the inelastic hinges of the roof. Under these hypotheses, the EDR is evaluated by performing nonlinear Time History analyses based on the cyclic behavior of the inelastic hinges of the roof, the strain energy contribution due to the walls, and the lateral displacements of the structure. The EDR values obtained with the Time History method are compared with those obtained by applying the Capacity Spectrum Method by performing nonlinear static analyses, either for the coefficient method of FEMA 356 or the equivalent linearization technique of ATC-40. The EDR evaluations are performed by considering the following different hysteretic behaviors of the roof's steel connections: the skeleton curves with stiffness degradation and the trilinear model with strength and stiffness degradation. Finally, the variation in the EDR values as a function of the hysteretic variable is presented as well so to evaluate if the maximum EDR value corresponds to the optimal value of the hysteretic variable able to reduce the lateral displacements and to contain the shear forces acting on the roof and the façade under a safety limit.

Keywords: historical buildings; churches retrofitting; cross-lam timber structure; equivalent damping; seismic vulnerability; nave transversal response

check for updates

Academic Editor: Maria Favvata

Received: 31 January 2025
Revised: 7 March 2025
Accepted: 13 March 2025
Published: 17 March 2025

Citation: Longarini, N.; Crespi, P.; Zucca, M.; Scamardo, M. Numerical Evaluation of the Equivalent Damping Ratio Due to Dissipative Roof Structure in the Retrofit of Historical Churches. *Appl. Sci.* **2025**, *15*, 3286. https://doi.org/10.3390/app15063286

1. Introduction

Historical single-nave masonry churches are mostly affected by the seismic action acting transversally with respect to the longitudinal axis of the nave. In fact, their dynamic behavior is generally characterized by a principal vibration mode shape that involves a high percentage of the total mass of the structure along the transversal direction. Therefore, the transversal response of the nave must be evaluated (i) to avoid the out-of-plane rocking mechanism of the perimeter walls and (ii) to limit the in-plane shear stresses acting on the wood roof elements and the façade [1–3]. In the retrofit design phase of single-nave churches, an effective dissipative roof diaphragm could represent a valid structural solution to improve the seismic response by achieving a global box behavior, thus avoiding the local mechanisms that can lead to the collapse of the structure. In this phase, solutions based on the use of original materials are very often preferable [4]. For historical churches, among the wood-based solutions, cross-laminated timber (CLT) panels, plywood panels, or inclined hardwood planks with respect to the pre-existing planks [3,5,6] can be considered for the retrofit of the roof, along with opportunely calibrated steel connections in terms of the strength and stiffness, with the aim of controlling the horizontal displacements on top of the walls. The calibration of the steel connections is related to the roof technology, the type of steel connections, and the connection layout. It is worth nothing that an over-strength and over-stiffness configuration of the roof diaphragm can undoubtedly reduce the horizontal displacement but also increase the in-plane shear forces acting on the roof and the facade up to values that are not compatible with the bearing capacity of these elements. Therefore, the dissipation of the energy in the roof connections, as well as the equivalent viscous damping, depends on the inelastic properties of the steel connections to be designed [7]. For the aforementioned issues, the present research aims to compare numerical methods for estimating the equivalent viscous damping due to the dissipative roof structure in the nave transversal response of historical churches in terms of the equivalent damping ratio (EDR).

In the case of cultural heritage masonry structures, limit analysis methods are commonly used to evaluate the safety of existing structures against the activation of local predefined failure mechanisms [8,9]. On the other hand, when dealing with masonry structures that exhibit a box behavior or that have already been retrofitted to avoid the activation of local mechanisms, global assessment techniques are also available [10–13]. Among them, linear and nonlinear, static, or dynamic methods can be applied [14,15].

For the design of the structural retrofit, the EDR can represent a useful parameter to design the steel connections of the roof, depending on the characteristics of the wooden roof structure and masonry walls. At the same time, in the design phase, a significant computational effort could be required in case of the implementation of the inelastic properties of the masonry walls and the roof's connections in a 3D model. Thus, an equivalent finite element model (FEM) can be implemented using the approach described in [16,17]. The equivalent FEM is described in Section 2.1.

In Section 2.2, the nave transversal seismic response is described, considering the nonlinear behavior of the roof's connections and walls, as a function of a hysteretic variable ($\beta_{\text{-}HYS}$), which represents a design parameter combining the yielding strength of both the roof and the masonry walls [3,6,17,18]. By changing $\beta_{\text{-}HYS}$ in a suitable range of values, different design configurations of the roof's connections can be tested up to the determination of the optimal value of $\beta_{\text{-}HYS}$ that is able to minimize the top horizontal displacement of the walls, while also keeping the shear stresses in both the roof and the walls in a safe range. Section 2.3 shows two different hysteretic models that can be adopted to describe the cyclic behavior of the steel connections on the basis of the results of cyclic tests performed on panel-to-panel connections [19–25] or evaluated by [26]. The two considered hysteretic models are (i) the stiffness degrading (SD) and (ii) the strength and stiffness degrading (SSD) models. In the equivalent FEM, SD is implemented through the Clough model [21,27] and SSD is implemented with the Takeda Slip model [28].

Section 3.1 describes the EDR evaluation by using the Capacity Spectrum Method (CSM), performing nonlinear static analyses through the coefficient method of FEMA 356 [29] and the equivalent linearization technique of ATC-40 [30]. The EDR values are evaluated as a function of the hysteretic variable β_{-HYS}, allowing for the evaluation and selection of different possible configurations of the roof. Section 3.2 describes a proposed Time History numerical approach for the EDR evaluation. This is based on nonlinear dynamic analyses of the equivalent FEM subjected to transverse earthquake loading, represented by a set of seven spectrum-compatible accelerograms [31–33]. In this way, different values of the EDR are calculated for different values of the hysteretic variable β_{-HYS} so to simulate the response of the retrofitted structure for several alternative design configurations of the roof's connections.

Section 4.1 describes the case study used for the analyses and Section 4.2 presents the EDR values obtained by FEMA 356, ATC-40, and the Time History method. The results are expressed for different values of the hysteretic variable β_{-HYS} in order to identify the optimal value $\beta_{-HYS\text{-}opt}$ that is able to maximize the EDR. The optimal value of the hysteretic variable corresponds to a design configuration of the connections of the wood roof diaphragm. In Section 4.3, the seismic response of the structure is analyzed in terms of two ratios, considering the lateral top displacement and the shear on the façade, as a function of the hysteretic variable β_{-HYS} so to evaluate the optimum $\beta_{-HYS\text{-}opt}$. In Section 4.4., a comparison between the optimum values of the hysteretic variable is discussed to identify the most suitable configuration of the dissipative roof that is able to (i) maximize the equivalent damping in terms of the EDR, (ii) reduce the lateral top displacement so to prevent the overturning of the lateral walls, and (iii) limit the in-plane shear force on the façade. In this way, excessive computational efforts during the design phase could be avoided, and the configuration of the roof related to $\beta_{-HYS\text{-}opt}$ could be subsequently tested and validated in a more detailed FEM 3D model. Final considerations are listed in Section 5. The strategy at the base of the present study is shown in Figure 1.

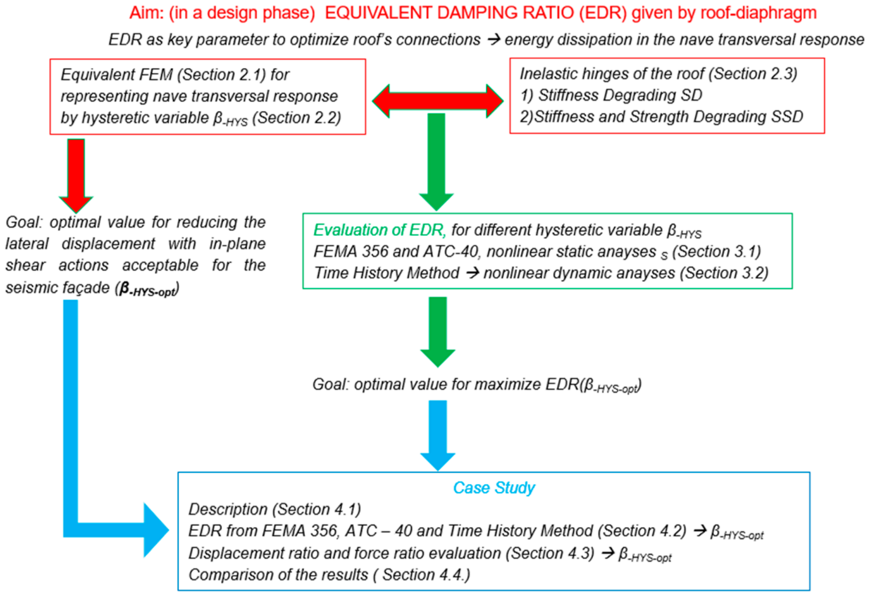

Figure 1. Strategy and structure of the proposed evaluation of the EDR.

2. Simulation of the Nave Transversal Response by Equivalent FEM

2.1. Equivalent FEM

The simulation of the transverse response of the historical church is carried out using an equivalent finite element model (FEM) representing the members of the structure involved in the nave transversal response [6,17,18] once the preliminary design of the roof diaphragm is defined (in terms of the thickness, material, and technology). In the equivalent FEM, the seismic action is introduced by means of a set of seven spectrum-compatible accelerograms acting perpendicularly to the nave axis [34,35]. In the FEM, the head and perimeter masonry walls are modeled as equivalent vertical beam elements, while the wooden roof with the related steel connections is introduced through horizontal beam elements. The geometries of the vertical elements reproduce the distribution of the masses of the walls, while the geometries that characterize the horizontal elements represent the thickness and length of the roof structures placed on top of the wooden trusses.

The dead loads of the roof are considered as distributed loads applied on the horizontal beam elements. The self-weight of the equivalent structure implemented in the FEM should correspond to the real one. The presence of the live and snow loads is not considered. The model was validated by verifying that the resultant of the applied loads matched the summation of the applied loads. Rotational inelastic hinges are introduced at the base of the vertical equivalent elements, while the façade and the head wall are considered as elastic elements, given their high in-plane strength and stiffness [18]. All of the vertical equivalent elements are fully fixed at the base node. The inelastic rotational hinges are described in terms of moment–rotation (M-φ) diagrams.

In the FEM, the roof diaphragm is represented by horizontal mono-dimensional equivalent elements linked to the vertical elements by hinges located at the top end of the vertical elements so to allow the rocking's trigger and to release the bending moment transferred to the roof. Both ends of the wood roof diaphragm are pinned to the head wall and façade. The inelastic properties of the connections of the roof are introduced in the FEM by in-plane shear hinges described by shear deformation (V-η) diagrams. This allows us to model the roof structure as a deformable roof diaphragm. Thus, the rocking trigger of the perimeter walls is allowed, but both the lateral top displacements and the in-plane shear forces acting on wooden-based pitched panels, the head wall, and the façade are limited only if the stiffness of the roof is opportunely calibrated [3,18]. In this way, the roof diaphragm can work as a damper on top of the church [36].

2.2. Simulation of the Nave Transversal Response

In a single-nave church, it is mandatory to identify the seismic-resisting elements under transversal earthquake in order to describe the nave transversal response. In the FEM, the structural macro-systems capable of withstanding the transversal earthquake are reproduced as equivalent beam elements. These include the head wall, the façade, and the coupled perimeter walls or the triumphal arches. The head wall and façade are directly reproduced in the FEM by vertical equivalent elements having the same geometry, the equivalent cross-section areas and inertia moment, and with a perfect restraint applied to the base node. The features of the coupled perimeter walls or triumphal arches are defined considering the geometrical and mechanical features of the walls of their relative sub-structures, as is explained in [6,17,18,37]. For example, in the case of the perimeter walls, each sub-structure is represented by the masonry pier included between two adjacent openings or the part of the wall belonging to a single abutment. For the triumphal arch, the sub-structures are the two columns or the two abutments with the relative part of the walls, depending on the as-built geometry of the church.

Naming the generic transversal seismic-resistant system as the “frame”, on the basis of the hypothesis made for the mechanical behavior of the structural elements, it behaves as a bilinear curve described by the yielding and ultimate force ($F_{frame,y}$ and $F_{frame,u}$, respectively) related to the yielding and the ultimate displacements ($\delta_{frame,y}$ and $\delta_{frame,u}$). The frame’s stiffness k_{frame} is obtained as the ratio between $F_{frame,y}$ and $\delta_{frame,y}$. The roof structure is characterized by a dissipative hysteretic behavior represented by an elastic–plastic curve, where the yielding and ultimate forces are $F_{roof,y}$ and $F_{roof,u}$, respectively, whereas the related yielding and ultimate displacements are $\delta_{roof,y}$ and $\delta_{roof,u}$. These values can be determined from experimental tests on the chosen connectors [24]. The stiffness of the roof k_{roof} is given by the ratio between $F_{roof,y}$ and $\delta_{roof,y}$. By changing the features of the roof’s connections, k_{roof} changes as well.

On the basis of these hypotheses, the nave transversal response of the church with the dissipative roof diaphragm can be represented by a flag-shaped diagram (Figure 2) in terms of the base shear versus the top displacement.

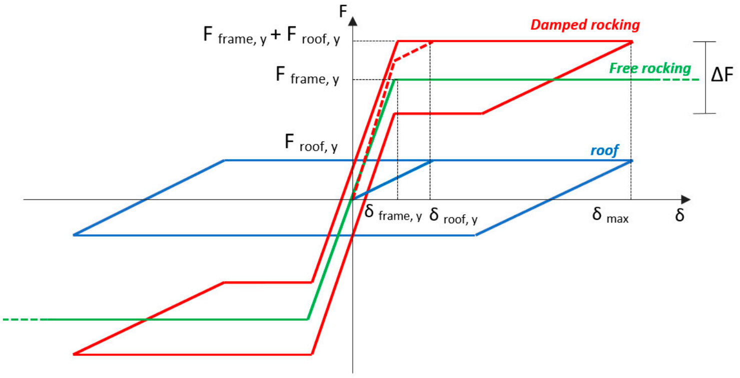

Figure 2. Representation of the nave transversal response by the flag-shaped diagram.

In a design phase, an index of the energy dissipated in the connections of the roof diaphragm is given by the hysteretic variable $\beta_{\text{-}HYS}$ [17]. When $\beta_{\text{-}HYS}$ increases, the damping effect also increases. The hysteretic variable links the inelastic properties of the masonry walls to the mechanical characteristic of the roof, as shown in Equation (1). The $\beta_{\text{-}HYS}$ optimal value is usually comprised in the range $\beta_{\text{-}HYS}$ = 0–1.5 because, for higher values, the self-centering rocking behavior is partially inhibited by the large residual displacements implied by the flag-shaped load–displacement diagram. In the design phase, it could also be interesting to test the seismic response beyond $\beta_{\text{-}HYS}$ = 1.5 [3,6,37] so to understand the effects of an over-stiffness and over-strength configuration of the roof on the overall structural response.

It should be remarked that an over-stiffness and over-strength roof configuration can have a negative effect on the transversal nave response of historic churches. In fact, in this case, the dissipative effect of the connections is reduced, allowing the roof to transfer a high value of in-plane shear force to the masonry of the façade and head wall. Consequently, the in-plane shear force acting on these macro-elements may not be acceptable in relation to the mechanical properties of the masonry.

Furthermore, in the absence of adequate dissipation, the shear force acting in the plane of the roof may be compatible with the mechanical properties of the steel connections, but not with the wood technology characterizing the pitched panels of the roof. It may therefore be necessary to increase the thickness of these wooden panels (whether they are double planks or cross-laminated timber), thereby increasing the masses involved in the seismic response and, consequently, with higher inertial forces.

By varying $\beta_{\text{-}HYS}$, and knowing $F_{frame,y}$ from the mechanical properties of the lateral walls, $F_{roof,y}$ is evaluated by Equation (2). Consequently, the stiffness of the roof k_{roof} can be expressed in terms of $\beta_{\text{-}HYS}$ using Equation (3). Defining Δ as the ratio between the yielding displacements of the roof and the frame (Equation (4)), the roof's stiffness k_{roof} is given by Equation (5). Thus, the roof structure designed in this way allows us to obtain a controlled rocking of the building characterized by a global seismic response with a flag-shaped diagram (Figure 2).

In a preliminary design phase, it is useful to consider the role of the ratio Δ. If $\Delta < 1$, in the nave transversal response, the roof reaches its yielding point before the activation of the rocking of the masonry walls. This means that the energy dissipation begins with the walls in their elastic field, while achieving possible damages in the structural elements of the roof. Therefore, it is preferable not to consider this option in the design phase. If $\Delta = 1$, the roof diaphragm and perimeter masonry walls will reach their relative yielding points simultaneously; thus, the energy dissipation due to the roof starts only if the rocking of the walls is uncontrolled. Otherwise, if $\Delta > 1$, the perimeter walls achieve the yielding point before the plasticization of the roof diaphragm. Notice that Δ values greater than one could be acceptable even if, for large Δ values, the energy dissipation in the roof elements will be activated only after the onset of dangerous lateral displacements at the top of the perimeter walls. In the following analyses, $\Delta = 1$ is considered as a preliminary design criterion.

$$\beta_{-HYS} = 2\,\frac{F_{roof,y}}{F_{frame,y}} \tag{1}$$

$$F_{roof,y} = \frac{\left(F_{frame,y} \cdot \beta_{-HYS}\right)}{2} \tag{2}$$

$$k_{roof,y} = k_{frame,y} \cdot \frac{\beta_{-HYS} \cdot \delta_{frame,y}}{2 \cdot \delta_{roof,y}} \tag{3}$$

$$\Delta = \frac{\delta_{roof,\,y}}{\delta_{frame,y}} \tag{4}$$

$$k_{roof} = \frac{\beta_{-HYS} \cdot k_{frame}}{2 \cdot \Delta} \tag{5}$$

Different configurations of the roof diaphragm are tested by performing nonlinear dynamic analyses [26,37]. The optimum roof stiffness should be calibrated by changing $\beta_{\text{-}HYS}$ up to its optimal value $\beta_{\text{-}HYS\text{-}opt}$, which is reached when the top lateral displacement is lower than the design value (i.e., 0.5% of the height of the perimeter walls according to [6,36]) and the in-plane stresses on the wooden roof diaphragm and the façade are compatible with the corresponding strengths. When $\beta_{\text{-}HYS\text{-}opt}$ is determined, the corresponding roof's stiffness is calculated with Equation (6), where k_{df} is the bending stiffness and k_{dt} is the shear stiffness. In Equation (6), given the presence of wooden elements and steel connections, the equivalent elastic modulus $E_w{}^*$, the equivalent shear modulus $G_w{}^*$, and the ideal inertia moment of the section $J_{id}{}^*$ are introduced and evaluated by Equations (7)–(9) [16,36], respectively. Therefore, every feature of the roof diaphragm (the geometry, material, and connections) are described by Equations (6)–(10), as follows:

$$k_{roof-opt} = \left(\frac{1}{k_{df}} + \frac{1}{k_{dt}}\right)^{-1} = \left(\frac{5}{6}\frac{L^3}{E_w^* J_{id}} + \frac{\chi L}{G_w^* A^*}\right)^{-1} \tag{6}$$

$$E_w^*(n_n, n_s) = \frac{\frac{L k_n}{n_s}}{2\frac{\frac{t_w L_y}{cos\alpha}}{n_n} + \frac{k_n \frac{L}{n_s}}{E_w}} \tag{7}$$

$$G_w^*(n_n, n_s) = \frac{\frac{L \cdot k_n}{n_s}}{2\frac{\frac{t_w \cdot L_y}{cos\alpha}}{n_n} + \frac{k_n \cdot \frac{L}{n_s}}{G_w}} \tag{8}$$

$$J_{id}^*(n_n, n_s) = \frac{t_w \cdot L_y^3}{12cos\alpha} + n_{ws} \cdot \left[2A_s\left(\frac{L_y}{2}\right)^2\right] \tag{9}$$

where

- n_{ws} is the homogenization coefficient of the steel-to-wooden diaphragm connection, given by $n_{ws} = E_s/E_w{}^*$ (where E_s is the steel elastic modulus);
- L is the distance between the seismic-resistant elements (the spacing between the transversal frames);
- L_y is the width of the roof;
- i is the spacing of the connectors;
- k_n is the stiffness of a single connector;
- t_w is the thickness of the wooden panels;
- $\chi = 6/5cos^2\alpha$ is the shear factor of the cross-section ($\chi = 1.2$ for rectangular sections);
- A_w is the cross-section area of the roof diaphragm;
- A^* is the shear area given by Equation (10), as follows:

$$A^* = \frac{A_w}{\chi} = \frac{\frac{t_w L_y}{cos\alpha}}{\frac{6}{5cos^2\alpha}} \tag{10}$$

- n_n is the number of connectors for each connection stripe (the ratio between the spacing of the seismic elements and the spacing of the connectors);
- n_s is the number of the connection stripes for each span;
- A_s is the cross-section area of the thin steel stripes of the roof diaphragm.

2.3. Hysteretic Models for the Roof's Connections

The hysteretic constitutive laws introduced in Section 2.2 and assigned to the inelastic hinges of the roof should be preliminarily defined to highlight their influence on the EDR, due to the change in the enclosed area of the hysteretic loops developed during the transversal response caused by the ground shaking. FEMA 356 [29], FEMA 440 [7], and ATC-40 [30] consider four hysteretic models, namely, (i) Elastoplastic Perfectly Plastic (EPP), (ii) Stiffness Degrading (SD), (iii) Strength and Stiffness Degrading (SSD), and (iv) Nonlinear Elastic (NE). The shape of the EPP hysteretic model does not correspond to the cyclic load–displacement behavior shown by the steel connections in the wooden elements [27], and the NE model does not exhibit hysteretic energy dissipation. Therefore, these two models are not considered for this application. The SD model corresponds to a model in which the lateral stiffness decreases when the lateral displacement increases [38]. Instead, the SSD model describes a cyclic behavior where both the lateral strength and lateral stiffness decrease when subjected to cyclic reversals. The load–displacement cycles of typical nailed or screwed panel-to-panel connections in the shear experimental tests on wood specimens can be placed halfway between the SD and SSD models [27,39]. Therefore, both the SD and SSD models are tested in the present numerical research by adopting the Clough model [38,40–42] for the SD model and the Takeda Slip model [43] for the SSD model, as shown in Figure 3. The adoption of the SD or SSD models is required to describe the cyclic behavior of the steel connections of the roof, depending on the characteristics of the connection and, possibly, based on the cyclic shear tests on the samples of the designed joint.

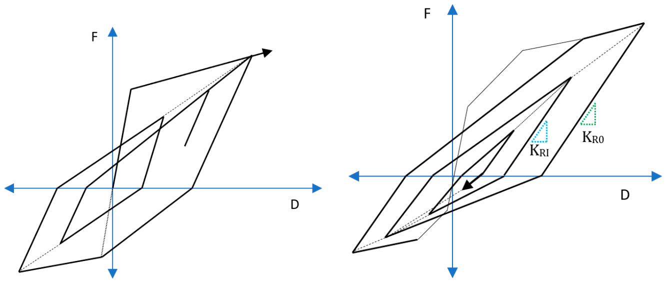

Figure 3. The Clough model used for the SD model (**left**) and the Takeda Slip model used for the SSD model (**right**).

3. Methods for EDR Evaluation

3.1. Equivalent Damping Ratio (EDR) in Capacity Sptectrum Method (CSM)

The equivalent damping ratio is a parameter used to evaluate the equivalent viscous damping of the dissipative roof structure. Equivalent viscous damping was first proposed in [8] and extended to the yielding of single-degree-of-freedom systems in [44,45]. Furthermore, several methods for the EDR evaluation have been proposed in [40,46]. The EDR can be evaluated by nonlinear static analyses (pushover analysis, PO), a type of analysis capable of evaluating the capacity of the structure and identifying the most stressed structural elements. In PO, the approaches of the coefficient method of FEMA 356 [7,29] and equivalent linearization technique of ATC-40 [30] are considered. In FEMA 356, the EDR is indicated by the symbol β_{eq}, while, in ATC-40, the EDR is referred to as the Effective Viscous Damping (β_{eff}). In both FEMA 356 and ATC-40, the hysteretic behavior of the structure is responsible for the dissipation of the energy due to the earthquake [47]. The energy dissipated in the hysteresis loops can be measured by the area enclosed in the hysteresis loops themselves. This area can be used for the determination of the Equivalent Viscous Damping. For the EDR evaluation, the equivalent FEM, described in Section 2, can be adopted, and the inherent damping of the structure should also be considered.

PO allows us to obtain the capacity curve of the structure in terms of the base shear versus the top displacement of the structure. This curve can then be converted into its corresponding spectral acceleration (S_a) versus spectral displacement (S_d) diagram by adopting the Capacity Spectrum Methods (CSMs) of FEMA and ATC-40. The CSM graphically plots the capacity curve in the S_a-S_d plane and is very useful because it gives a clear graphical representation of the nonlinear behavior of the structure. To obtain the capacity curve in the S_a-S_d plane, the equivalent linearization method [30] or coefficient method [29] can be adopted. When the capacity curve is plotted in the S_a-S_d plane, the following two response spectra could be represented in the same plane: (i) the elastic spectrum (considering only the inherent viscous damping of the structure) and (ii) the inelastic spectrum (related to the total damping). The value of the inherent damping depends on the materials properties, but, in [48], it is considered equal to 5% for all types of structures, although it could be set to 3% for steel structures [49] and between 3% and 5% for unreinforced masonry structures [50]. In this work, 5% will be considered.

A graphical representation of the use of the CSM for the evaluation of the equivalent viscous damping is given in Figure 4, where a_y and d_y define the linear branch of the bilinearized capacity curve, while a_{pi} and d_{pi} represent the coordinates of the performance point (PP, the intersection between the capacity curve and the inelastic spectrum), with d_{pi} being the maximum inelastic displacement of the structure.

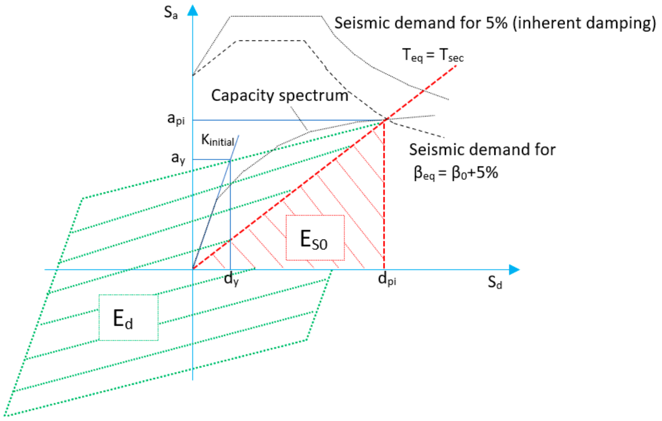

Figure 4. EDR representation in the Capacity Spectrum Method.

When the equivalent linearization method of ATC-40 is adopted, the EDR is evaluated by Equation (11), where E_d is the dissipated plastic energy (corresponding to the area enclosed by the hysteresis loop) and E_{S0} is the maximum elastic strain energy (graphically represented by the area of the triangle defined by the spectral displacement d_{pi} and the spectral acceleration a_{pi} of the PP). The EDR is obtained by considering the sum of the inherent damping (5%) and the hysteretic damping represented as the equivalent viscous damping (β_0).

When the coefficient method of FEMA 356 is adopted, the EDR is evaluated by Equation (12), depending on the ductility ratio μ, the post-yield stiffness ratio α, and an adjustment factor k considering changes in the hysteretic behavior. In FEMA 356, the EDR is indicated as β_{eff}, and it is calculated as the sum of the inherent damping (5%) and a term representing the dissipated energy in the form of the equivalent viscous damping (β_0).

$$EDR = 5\% + \frac{1}{4\pi}\left(\frac{E_d}{E_{S0}}\right) = 5\% + \beta_0 \tag{11}$$

$$EDR = 5\% + k\cdot\frac{2}{\pi}\cdot\left(\frac{(\mu-1)\cdot(1-\alpha)}{(\mu\cdot(1+\alpha\cdot\mu-\alpha)}\right) = 5\% + \beta_0 \tag{12}$$

Since the structure can dissipate energy by the inelastic hinges present in the equivalent elements of the FEM, it is mandatory to evaluate the capacity curve and the corresponding EDR for the different possible behaviors of the connections present in the roof by considering the different hysteretic models already described. ATC-40 reports the following three kinds of structural behaviors: (i) Type A, (ii) Type B, and (iii) Type C, corresponding to the (i) EEP, (ii) SD, and (iii) SSD hysteretic models of FEMA 440, respectively. As previously anticipated, the EEP model is not considered in this work. If Type B is adopted, the Clough model (SD) is attributed to the inelastic hinges of the roof, and, in Equation (12), $k = 0.67$ [29]. If Type C is adopted, the Takeda Slip model (SSD) is attributed to the inelastic hinges of the roof so to consider the stiffness and strength degradation, and, in Equation (12), $k = 0.33$ [29].

3.2. Time History Method for EDR Evaluation

The Time History (TH) method is based on the use of seven spectrum-compatible accelerograms as the seismic action. The response of the roof is represented by hysteretic cycles developed in the shear inelastic hinges applied to the roof elements (adopting the SD or SSD models; see Figure 5a,b). The response of the masonry walls is described by elastic bilinear diagrams [37,51–53] for the inelastic rotational hinges located at the base of the vertical equivalent elements of the resistant frames, as shown in Figure 5c. In both the

SD and SSD models, each inelastic hinge is able to dissipate energy and shows different closed cycles during the seismic event.

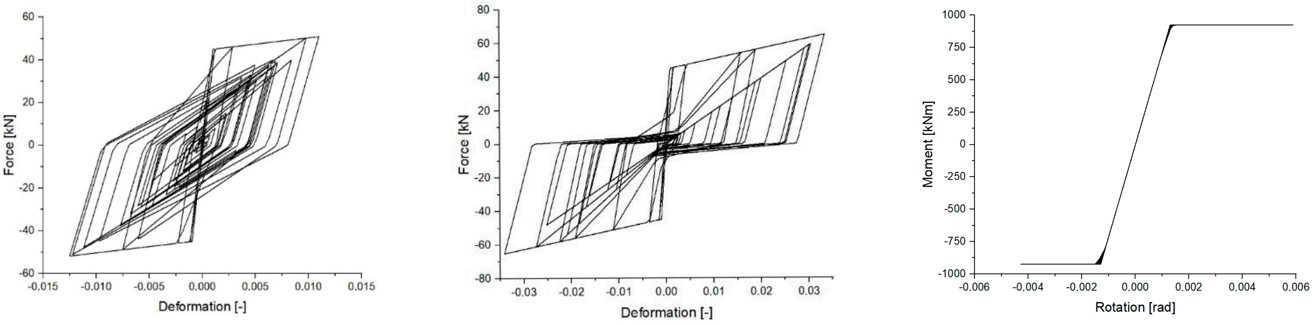

(**a**) (**b**) (**c**)

Figure 5. Examples of the hysteretic cycles of different inelastic hinges: (**a**) roof SD model, (**b**) roof SSD model, and (**c**) masonry NE model.

Once the control node of the structure is defined as the node located in the center of mass at the roof level in the FEM [29], the church's response in terms of the top lateral displacement can be plotted as a function of time. Then, a full hysteretic cycle, defined by the points 0 ÷ 4, as shown in Figure 6, can be extracted from the whole response of the structure. Considering seven spectrum-compatible accelerograms, the process is applied seven times, and the average value can be considered.

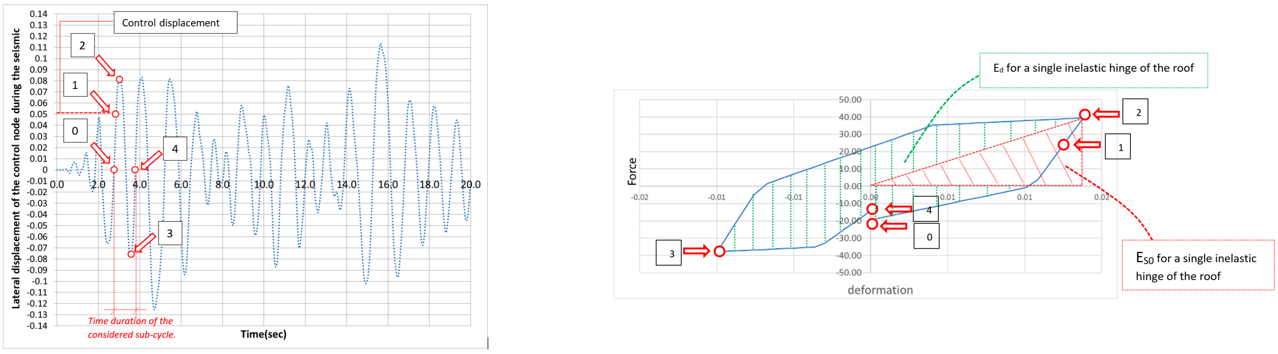

(**a**) (**b**)

Figure 6. (**a**) The cycle extracted from the Time History of the lateral top displacement of the roof's central node; (**b**) the corresponding sub-cycle of a roof inelastic hinge for the evaluation of the energies (E_D and E_{S0}).

The selection of the hysteretic cycle is illustrated in Figure 6. The first instant corresponds to the one in which the control node achieves the control displacement design value for the first time during the seismic event, namely, point 1 in Figure 6a. It must be underlined that FEMA 356 and ATC-40 could result in different control displacement values. The control displacement identifies a target value at which the structure reaches a predefined performance level, such as the yielding of the vertical elements representing the walls [7,29,30]. Then, the starting point of the cycle (point 0 in Figure 6a) is located immediately before point 1 on the time axis. The following instants correspond to the maximum transversal displacements in both the positive and negative directions (points 2 and 3 in Figure 6a). The last instant represents the end point of the cycle, occurring when the displacement's Time History crosses the time axis again (point 4 in Figure 6a). When the time window identifying the cycle is determined (from point 0 to point 4 instants), all of the corresponding sub-cycles of the roof inelastic hinges can be extracted for the energy calculation. Moreover, the time instants (corresponding to 0 ÷ 4 points) can be used to determine the branches of the bilinear responses of the inelastic hinges of the walls' equivalent elements. Their contribution in terms of strain energy will be considered in the evaluation of the global EDR of the structure.

For each inelastic hinge present on the roof, a force–displacement loop is extracted for the selected time window (0 ÷ 4 points). This corresponds to a sub-cycle of the complete cycling history of the i-th roof inelastic hinge (Figure 6b), and its enclosed area represents the hysteretic energy dissipated by the i-th inelastic hinge ($E_{D,i}$). When the sub-cycle is plotted, the maximum transversal displacements can be detected along the positive and negative seismic directions. In correspondence of the absolute maximum displacement value, the maximum strain energy ($E_{S0,i}$) of the force–displacement sub-cycle can also be calculated. In the case where the inelastic hinges are in the elastic range, they do not give a contribute in terms of damping energy, i.e., $E_{D,i} = 0$. However, in these cases, the inelastic hinges are considered either way in terms of their strain energy contributions ($E_{S0,i}$).

Therefore, by considering the inelastic hinges of the walls and roof, the EDR of the structure in the nave transversal response under the seismic action can be estimated by Equation (13), where n represents the total number of inelastic hinges of the roof and the walls, and $E_{D,i}$ and $E_{S0,i}$ indicate, respectively, the dissipated energy and the maximum strain energy of the i-th inelastic hinge in the time window extracted from the overall displacement Time History of the control node. The graphical procedure illustrated in the previous figure (Figure 4) for the Capacity Spectrum Method is performed for all of the inelastic hinges under the seven spectrum-compatible accelerograms. The values to be considered for the EDR calculation are the average ones. Thus, in Equation (13), $E_{D,i}$ and $E_{S0,i}$ are the average values. The analyses are carried out by Midas Gen [54].

$$EDR = 5\% + \frac{1}{4\pi}\frac{\sum_{i=1}^{n} E_{D,i}}{\sum_{i=1}^{n} E_{S0,i}} \tag{13}$$

4. Case Study

4.1. Description of the Case Study

The nonlinear dynamic analyses and EDR evaluation are performed for a case study represented by a single-nave church with masonry walls and a wooden roof modeled with the equivalent FEM. The church has a 33 × 12 m rectangular plan, 90 cm thickness head and façade walls, and 60 cm thickness perimeter walls, while the roof structure is composed of hardwood trusses (horizontal tie beam elements with a 17 × 17 cm section, inclined principal rafters with a 30 × 18 cm section, struts with a 12 × 17 cm section, and a king post with a 12 × 12 cm section), joists (12 × 16 cm section), and 3.5 cm thick planks. The 3D initial model and the equivalent FEM with inelastic features are shown in Figure 7. The masonry is characterized by Young's modulus E = 1200 MPa and a density ρ = 18 kN/m^3. The hardwood elements are characterized by Young's modulus parallel to the fibers $E_{0,mean}$ = 10,000 MPa, a shear modulus G_{mean} = 630 MPa, a tensile strength parallel to the fibers $f_{t,0,k}$ = 20 MPa, and a density ρ_w = 5.00 kN/m^3.

Starting from the design target behavior, in which the yielding of the steel connections of the roof and the yielding of the inelastic hinges of the walls are activated simultaneously (Δ = 1; Equation (4)), the properties of the roof inelastic hinges vary as a function of the hysteretic variable $\beta_{\text{-}HYS}$. Table 1 reports the inelastic hinge properties for the resistant frames (corresponding to the piers of the lateral walls) and the roof. To consider several possible configurations of the proposed retrofitting of the roof, seven different cases were analyzed. Starting from the capacity of the masonry walls, evaluated according to [6,17,18], which cannot be changed, different values of the hysteretic variable $\beta_{\text{-}HYS}$ were taken into account and, consequently, the yield load of the roof connections was defined according to Equation (2). Then, by assuming $\Delta = 1$ (Equation (4)), the stiffness of the roof can be determined. Consequently, by knowing the stiffness of the roof, the mechanical properties of the wood panels, and the geometrical features of the church, the design of the steel connections can be carried out using Equations (6)–(10). The ultimate over-yielding force ratio of the roof elements was assumed to be 1.25 on average according to experimental tests performed by [24].

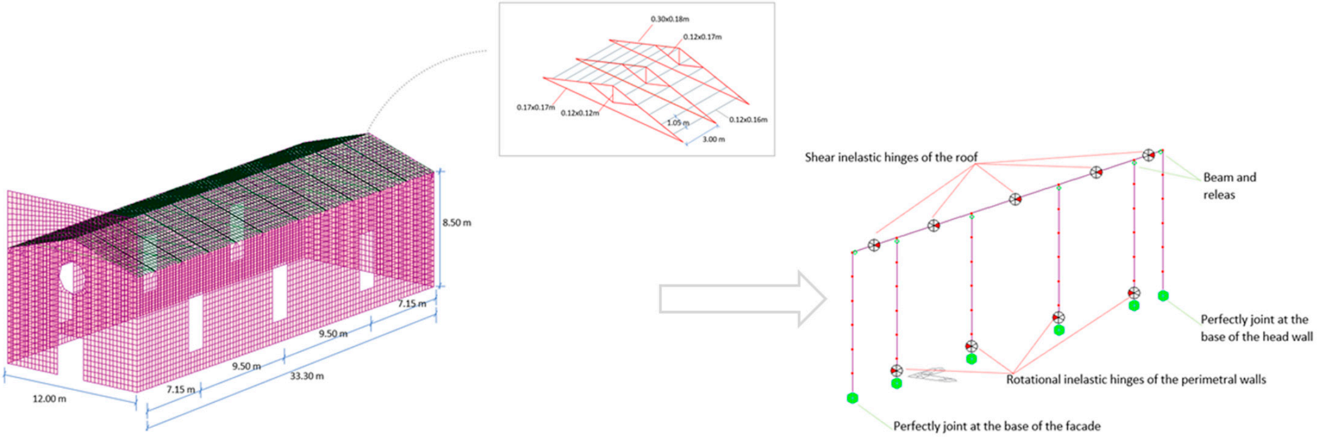

Figure 7. Case study: geometries and equivalent frame FEM.

Table 1. Properties of the inelastic hinges for the SD model (Clough). Note: P1-D1 in the SSD model are 10% less than P1-D1 of the SD model. P2-D2 in the SSD model corresponds to P1-D1 of the SD model. P3-D3 in the SSD model corresponds to P2-D2 of the SD model.

Parts of the Roof Close to the Head Wall and Facade							
$\beta_{\text{-}HYS}$	P_1 [kN] = $F_{roof,y}$	P_2 [kN] = $F_{roof,u}$	$D_1 = (P_1/K_{roof,y})/L$	D_2	$M_{frame,y} = M_{frame,u}$ [kNm]	$R_{frame,y}$ [rad]	$R_{frame,u}$ [rad]
0.30	9.69	12.11	0.00062	0.01257	555.422	0.00086	0.00258
0.60	19.38	24.22	0.00062	0.01257	555.422	0.00086	0.00258
0.90	29.06	36.33	0.00062	0.01257	555.422	0.00086	0.00258
1.20	38.75	48.44	0.00062	0.01257	555.422	0.00086	0.00258
1.50	48.44	60.55	0.00062	0.01257	555.422	0.00086	0.00258
1.80	58.13	72.66	0.00062	0.01257	555.422	0.00086	0.00258
2.10	67.81	84.77	0.00062	0.01257	555.422	0.00086	0.00258
Central Parts of the Roof							
$\beta_{\text{-}HYS}$	P_1 [kN] = $F_{roof,y}$	P_2 [kN] = $F_{roof,u}$	$D_1 = (P_1/K_{roof,y})/L$	D_2	$M_{frame,y}= M_{frame,u}$ [kNm]	$R_{frame,y}$ [rad]	$R_{frame,u}$ [rad]
0.30	189.72	237.15	0.008619834	0.17239	10,877.185	0.01182	0.03548
0.60	379.44	474.30	0.008619834	0.17239	10,877.185	0.01182	0.03548
0.90	569.16	711.44	0.008619834	0.17239	10,877.185	0.01182	0.03548
1.20	758.87	948.59	0.008619834	0.17239	10,877.185	0.01182	0.03548
1.50	948.59	1185.74	0.008619834	0.17239	10,877.185	0.01182	0.03548
1.80	1138.31	1422.89	0.008619834	0.17239	10,877.185	0.01182	0.03548
2.10	1328.03	1660.04	0.008619834	0.17239	10,877.185	0.01182	0.03548

Points P1-D1 and P2-D2 represent the yielding and ultimate points, respectively. For the inelastic hinges of the roof, if the SD model is adopted (the Clough model), P1 and P2 indicate the yielding and the ultimate force of the roof's inelastic hinges, respectively, and D1 and D2 are the dimensionless drifts given by the ratio between the yielding or the ultimate displacements and the length of the church. Otherwise, if the SSD model is adopted (Takeda slip model), three points, P1-D1, P2-D2, and P3-D3, should be defined to describe the inelastic hinge behavior. The Takeda model is normally used to represent the hysteretic behavior of reinforced concrete structures [43]. In the case of steel connections in a wooden structure, the Takeda model can also be adopted, but with some appropriate modifications [55]. It is possible to assume P2-D2 as the yielding point and P3-D3 as the ultimate point (as already evaluated for the SD model), while the P1-D1 values can be set to 90% of the yielding point [56,57].

In the case study, the design of the preliminary retrofit intervention on the roof considers pitched CLT panels with a thickness of 6 cm (characterized by three layers, each one with a 2 cm thickness and an elastic modulus $E_{CLT\text{-}0,mean}$ = 12 GPa, a shear modulus G_{CLT} = 690 MPa, a tensile strength parallel to the fibers $f_{CLT\text{-}t,0,k}$ = 18 MPa, and a density $\rho_{CLT\text{-}w}$ = 4.8 kN/m^3). The panels have a rectangular shape of 6.10 × 3.00 m and are placed between the wooden trusses.

In the FEM, the equivalent horizontal beam element modeling the roof diaphragm considers the panels' cross-section. In terms of the applied loads, the dead load related to the wooden trusses of the roof is implemented as uniform loads on the horizontal elements. Furthermore, the upper part of the façade is considered as an equivalent nodal load applied on the top node of the vertical equivalent element representing the façade. To account for the effect of the steel connections between the new CLT roof structure and the existing masonry walls, cylindrical hinges were placed at the intersection of the roof elements and the top of the walls. In the equivalent FEM, following this approach, rocking is allowed to occur and the bending moment transferred to the roof structure is released. Furthermore, the equivalent elements of the roof are also pinned to the head wall and façade equivalent members.

4.2. Results in Terms of EDR

FEMA 356 and ATC-40 are initially adopted with both the SD and SSD models for the hinges of the roof and to vary the hysteretic variable $\beta_{\text{-}HYS}$. The control node is set in the middle of the roof and its transversal displacement is plotted under the seven accelerograms. When the nonlinear static analyses (pushover) are performed, the values of the target control displacement changes in relation to the SD or SSD models, and it could be different in FEMA 356 and ATC-40. Table 2 shows the target displacement values for the different hysteretic variables.

Table 2. Target displacements of the control node by PO in FEMA 356 and ATC-40.

$\beta_{\text{-}HYS}$	Method	SD—Target Displacement [m]	SSD—Target Displacement [m]
0.3	PO-FEMA/PO-ATC	0.038/0.055	0.041/0.057
0.6	PO-FEMA/PO-ATC	0.028/0.051	0.030/0.056
0.9	PO-FEMA/PO-ATC	0.028/0.044	0.031/0.050
1.2	PO-FEMA/PO-ATC	0.027/0.045	0.030/0.050
1.5	PO-FEMA/PO-ATC	0.037/0.054	0.039/0.057
1.8	PO-FEMA/PO-ATC	0.036/0.051	0.035/0.050
2.1	PO-FEMA/PO-ATC	0.021/0.039	0.021/0.039

The Time History method (TH) is applied to the case study considering the control node's target displacements obtained by FEMA 356 and ATC-40. Seven spectrum-compatible accelerograms, selected by Rexel software v3.5 [35], simulating the L'Aquila earthquake [58], were considered. The main parameters characterizing the elastic spectrum of the considered site, according to the Italian design code [59], are the peak ground acceleration PGA = 0.30 g, the return period T_R = 475 years, the horizontal amplification factor F_o = 2.36, the vertical amplification factor F_v = 1.63, and the acceleration–velocity transition period T^*_c = 0.347 s.

The analyses are performed by varying the hysteretic variable $\beta_{\text{-}HYS}$ between 0 and 2.1. The Time History of the control node displacement is considered to select the time window of the reference cycle according to the procedure described in Section 3.2. Once the cycle is selected, the hysteresis loops of the inelastic hinges of the roof can be extracted, and the corresponding dissipated energy is calculated. Moreover, the bilinear behavior of the walls is detected as well, and the strain energy is computed and used for the evaluation of the EDR. This procedure is performed using both the SD and SSD models for comparison.

The EDR values obtained with the TH method by using the FEMA and ATC displacements of the reference point are plotted in Figures 8a and 8b, respectively. When the TH method is used with the equivalent FEM (Figure 9a), hysteretic loops are detected starting from the cyclic responses of the inelastic hinges of the roof (Figure 9b), while elastic–plastic bilinear cycles are identified for the walls (Figure 9c). In Figure 9a–c, for the sake of brevity, the cycles and the extraction of sub-cycles are shown only in correspondence of one of the seven accelerograms and for the SD model.

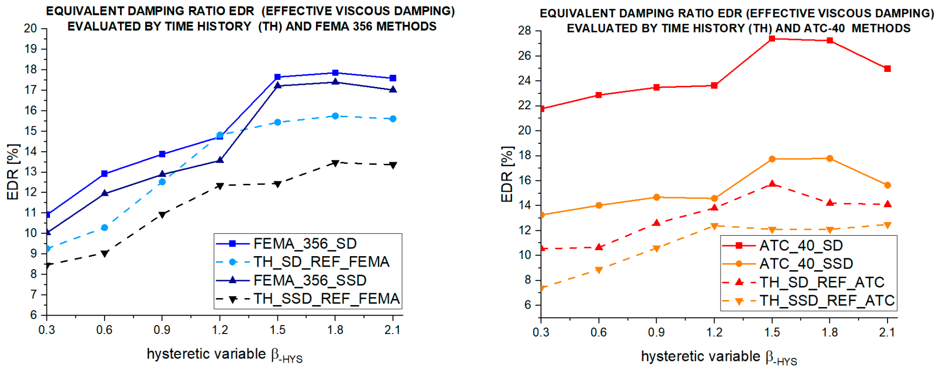

(**a**) (**b**)

Figure 8. EDR evaluation with the TH analyses as a function of $\beta_{\text{-}HYS}$ for (**a**) FEMA 356 and (**b**) ATC-40 for the SD and SSD models.

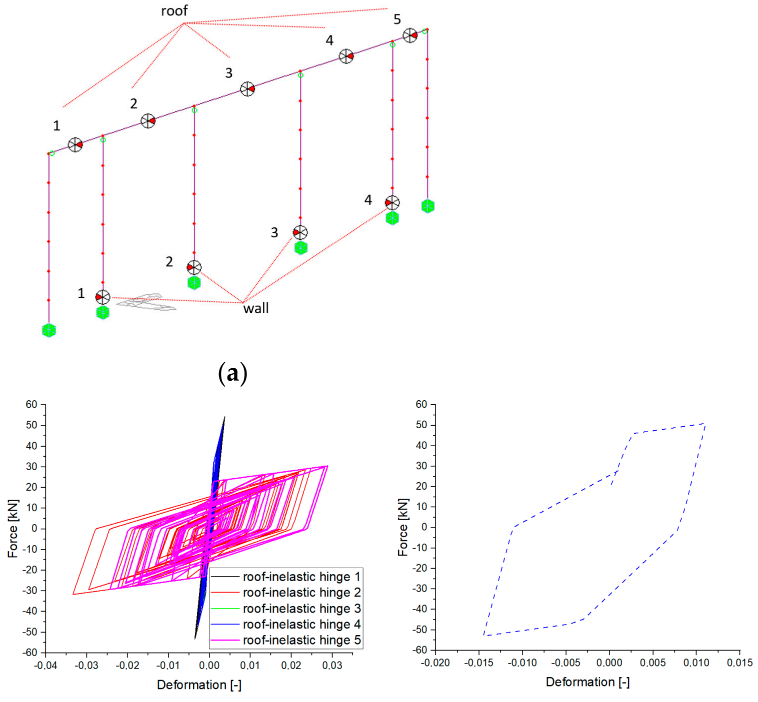

(**a**)

(**b**)

Figure 9. *Cont.*

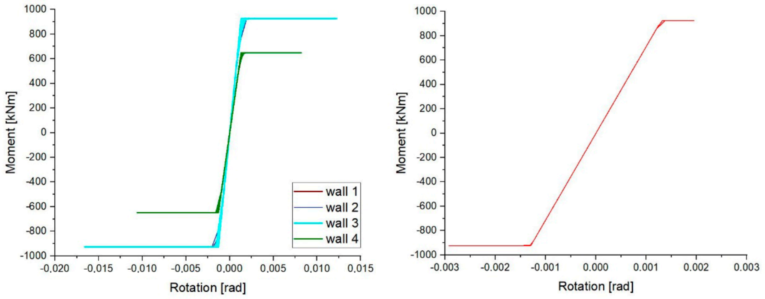

(**c**)

Figure 9. (**a**) The identification of the inelastic hinges in the FEM; (**b**) the cyclic responses of the roof's inelastic hinges (on the **left**) and an example of an extracted single loop for hinge 1 with the SD model under accelerogram 1 (on the **right**); (**c**) the elastic–plastic responses of the walls' inelastic hinges (on the **left**) and an example of an extracted single cycle for hinge 1 under accelerogram 1 (on the **right**).

4.3. Results in Terms of Damped Rocking

The seismic response of the case study is discussed by comparative analyses in terms of the damped rocking expressed in terms of the force ratio (RF) and the displacement ratio (RD), where

- The RF is the ratio between the shear force evaluated in the node connecting the roof to the façade in the equivalent FEM, and the total shear force evaluated at the base of the structure;
- The RD is defined as the ratio between the transversal displacement of the roof and the target displacement (chosen as the 0.5% of the total height of the perimeter walls).

As an example, the first vibration mode shape, either for the 3D model or the equivalent FEM, is depicted in Figure 10, from lateral and top views, to show the transverse deformation that involves a great part of the structure's mass. Concerning the equivalent FEM adopted for the analyses, the first twenty natural periods and the corresponding percentage of the masses involved in the vibrational mode shapes are shown in Table 3. Moreover, the status of the yielding of the inelastic hinges is shown in Figure 11 for one of the accelerograms at the end of the seismic event so to detect whether the hinges are beyond the elastic limit. When the optimal value of the hysteretic variable $\beta_{\text{-}HYS\text{-}opt}$ is reached (Section 2.2), it is possible to observe that the RD trend is the opposite of the RF one (Figure 12). When the value of $\beta_{\text{-}HYS}$ exceeds 1.5, the RD does not significantly decrease, as occurs for lower $\beta_{\text{-}HYS}$ values, while the RF continues to increase. This means that an overstiffness configuration is not recommendable in the roof structure optimization to avoid the onset of extreme shear actions on the façade. The RD and RF values plotted in Figure 12 are calculated as the average ones obtained for the seven spectrum-compatible accelerograms.

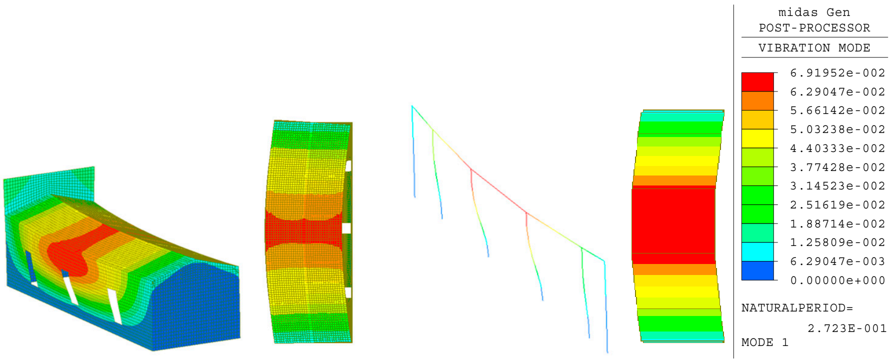

Figure 10. Deformed shape related to the first transversal vibrational mode for the 3D model (Iso and top views, **left**) and the equivalent FEM (Iso and top views, **right**).

Table 3. Case study: the features of the first twenty vibrational mode shapes (equivalent FEM).

Mode	Period	tran-x		tran-y		rotn-z	
n.°	[s]	Mass (%)	Sum (%)	Mass (%)	Sum (%)	Mass (%)	Sum (%)
1	0.271	58.54	58.54	0.00	0.00	0.03	0.03
2	0.185	0.00	58.54	39.78	39.78	0.00	0.03
3	0.183	0.13	58.67	0.00	39.78	39.12	39.15
4	0.179	0.00	58.67	0.07	39.85	0.00	39.15
5	0.175	5.96	64.63	0.00	39.85	0.05	39.20
6	0.174	0.01	64.64	0.00	39.85	4.00	43.20
7	0.123	2.25	66.89	0.00	39.85	0.00	43.20
8	0.116	0.00	66.89	35.40	75.25	0.00	43.20
9	0.092	0.01	66.91	0.00	75.25	24.12	67.33
10	0.076	15.19	82.09	0.00	75.25	0.30	67.63
11	0.073	0.00	82.09	0.01	75.26	0.00	67.63
12	0.063	0.01	82.11	0.00	75.26	8.41	76.04
13	0.057	0.00	82.11	7.01	82.27	0.00	76.04
14	0.056	2.37	84.48	0.00	82.27	5.17	81.20
15	0.055	3.05	87.53	0.00	82.27	5.62	86.82
16	0.055	0.00	87.53	0.02	82.29	0.00	86.82
17	0.051	0.00	87.53	0.45	82.74	0.00	86.82
18	0.050	3.23	90.76	0.00	82.74	0.01	86.83
19	0.048	0.00	90.76	0.00	82.74	0.00	86.83
20	0.047	0.00	90.76	0.00	82.74	0.00	86.83

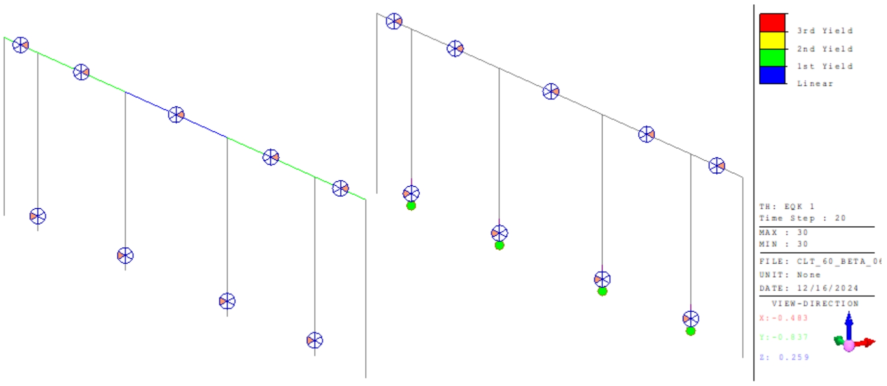

Figure 11. Status of the yielding of the roof's hinges (on the **left**) and the walls' hinges (on the **right**) at the end of one of the accelerograms.

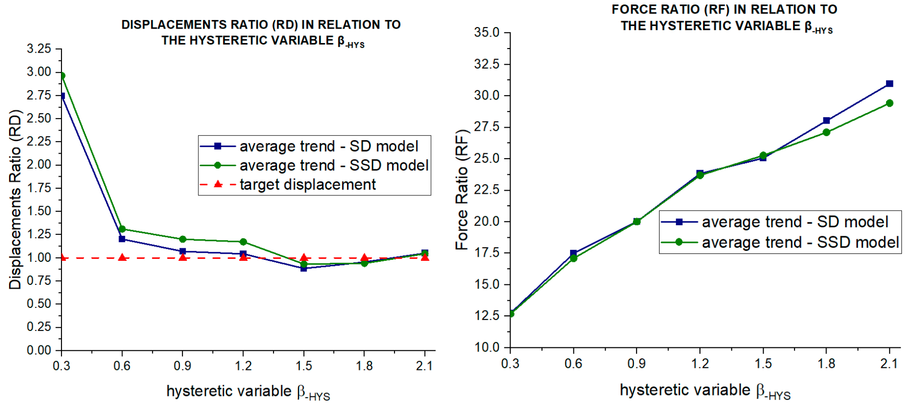

Figure 12. Average values of the displacement ratio (on the **left**) and force ratio (on the **right**) by varying the hysteretic variable $\beta_{\text{-}HYS}$.

4.4. Remarks

The analyses performed on the retrofitted church configurations showed that the EDR values determined using FEMA 356 or ATC-40 were generally higher than those calculated with the TH method. The influence of the hysteretic model (SD and SSD) adopted for the inelastic hinges of the roof is clear, with a lower damping coefficient in the case of the SSD model. This seems justified by the lower amount of energy dissipated by the roof connections during the seismic event due to the narrower shape of the hysteretic loops that characterize the SSD model, regardless of the trends of the accelerograms. In the EDR evaluation, the value of the hysteretic variable $\beta_{\text{-}HYS\text{-}opt}$, corresponding to the maximum EDR, is close to its limit value of $\beta_{\text{-}HYS\text{-}opt} = 1.5$. Beyond this value, the EDR curve is essentially flat and, indeed, towards the value of $\beta_{\text{-}HYS\text{-}opt} = 2.1$, the EDR begins to decrease. For the case study, in the design phase, $\beta_{\text{-}HYS\text{-}opt} = 2.1$ represents an extremely rigid configuration of the connections. On the other hand, in the nave transversal response of the case study analyzed in terms of the damped rocking by the introduction of the displacement ratio and force ratio, the optimal value of the hysteretic variable is about $\beta_{\text{-}HYS\text{-}opt} = 1.40$.

Since the evaluation of the EDR and the damped rocking analyses gave very similar results in terms of the hysteretic variable, it is possible to compare the EDR values for $\beta_{\text{-}HYS\text{-}opt} = 1.40$, calculated by FEMA 356, ATC-40, and the TH. In correspondence of $\beta_{\text{-}HYS\text{-}opt}$, including 5% of the inherent damping, the EDR evaluated with FEMA 356 is in the range between 16.00% and 16.80%, while, when considering ATC-40, it is in the range between 16.3% and 25%, for the SSD and SD models, respectively. The EDR values obtained for FEMA 356 and ATC-40 in correspondence of $\beta_{\text{-}HYS\text{-}opt}$ are listed in Table 4.

Table 4. EDR values for the case study for $\beta_{HYS\text{-}opt} = 1.40$.

Method	Model	EDR [%]
FEMA 356	SD	≃16.8
ATC-40	SD	≃25.0
TH in relation to FEMA 356	SD	≃15.2
TH in relation to ATC-40	SD	≃14.8
FEMA 356	SSD	≃16.0
ATC-40	SSD	≃16.3
TH in relation to FEMA 356	SSD	≃12.5
TH in relation to ATC-40	SSD	≃12.1

When FEMA 356 is adopted, the difference in the EDR values for the SD and SSD models is $\Delta_{FEMA\text{-}SD\text{-}SSD} = 5\%$, while, when considering ATC-40, the difference is $\Delta_{ATC\text{-}SD\text{-}SSD} = 53\%$. This could be a limit for these codes, which is due to the different approaches (the coefficient method and equivalent linearization method, respectively). When the TH method is adopted, the computed EDR values are much more homogeneous. In fact, when the cycle extracted in the TH method refers to FEMA 356, the difference between the EDR with the SD model and the one with the SSD model is $\Delta_{TH\text{-}FEMA\text{-}SD\text{-}SSD} \cong 21\%$, whereas, if the TH refers to ATC-40, the corresponding difference is $\Delta_{TH\text{-}ATC\text{-}SD\text{-}SSD} \cong 22\%$.

Moreover, when comparing the estimated EDR values obtained from the TH analyses and related to the selected cycles identified by the two codes for the same hysteretic cycle model, the following differences can be highlighted: (i) for the SD model, the difference between the EDR values based on FEMA 356 and ATC-40 is about 2.7%, while (ii), for the SSD model, the difference between the EDR values calculated using FEMA 356 and ATC-40 is about 3.3%. This means that, for the same hysteretic model, the EDR predictions obtained with the TH method are essentially independent of the code used to select the reference cycle.

By analyzing the EDR trend as a function of the hysteretic variable, for both the Capacity Spectrum Methods and the TH method, it is possible to notice that (i) the EDR shows a quasi-linear trend in the range $0.3 < \beta_{\text{-}HYS} < 1.2$, (ii) the EDR shows a spike in the range $1.2 < \beta_{\text{-}HYS} < 1.5$, and (iii) the energy dissipation due to the roof diaphragm is not significant once the EDR exceeds $\beta_{\text{-}HYS} = 1.5$. In fact, in the range $1.5 < \beta_{\text{-}HYS} < 2.1$, the EDR is almost constant, or it decreases, as occurs for ATC-40 and the TH method referring to ATC-40. This means that the design of an over-stiffness roof diaphragm does not represent a useful seismic solution to improving the transversal response of a historical single-nave church. This can be also extended to historical churches with a central nave and two lateral aisles when the first vibration mode shape is characterized by a significant percentage (about 50–60%) of the total mass of the construction.

The obtained EDR is related to the energy dissipation in the panel-to-panel and panel-to-wall steel connections. This energy dissipation is caused by the plasticization of the steel elements, which can be damaged during the earthquake. Therefore, after the seismic event, the steel connections should be inspected to verify their condition. Two scenarios can occur. The first scenario concerns a connection with only cylindrical shank elements (e.g., steel screws). In this case, the plasticization of the screws also implies the damage of the surrounding wood. Therefore, after the seismic event, a careful inspection of all of the CLT panels should be carried out and, in the case of panels that are too damaged, it may be necessary to replace some of them. In the second scenario, the connection usually also includes a thick perforated steel plate as a coupling strip. In this case, the connection behaves as an elastic–plastic device, where the screws remain in the elastic field, while the energy dissipation is localized in the perforated steel plate. As a consequence, after the post-earthquake inspection, only the substitution of the steel plate may be required. In both cases, the amount of damage in the masonry walls could be limited by the hysteretic behavior of the retrofitted roof structure.

5. Conclusions

This paper proposes numerical approaches for the evaluation of the equivalent damping ratio in the transversal response for a single-nave historical church due to wooden-based dissipative roof structures.

The present research aims to discuss different methods for estimating the dissipative effects of the roof diaphragm in terms of the EDR. Therefore, the EDR is evaluated for several roof configurations characterized by different values of the hysteretic variable $\beta_{\text{-}HYS}$. The analysis of the obtained results leads to the determination of an optimal value of the hysteretic variable $\beta_{\text{-}HYS\text{-}opt}$ that is able to maximize the EDR for the following two different possible behaviors of the steel connections: the stiffness degrading model or the strength and stiffness degrading model. The optimal value of the hysteretic variable $\beta_{\text{-}HYS\text{-}opt}$ identifies the structural configuration with the best seismic response and the maximum EDR value to be considered in the design of the steel connections of the roof. In this way, through complex nonlinear analyses, the optimal values of the hysteretic variable $\beta_{\text{-}HYS\text{-}opt}$ and the EDR can be evaluated. These values could represent reference parameters to be considered by designers when developing the design of retrofit interventions using linear analyses on common FEMs.

As a possible future development of the research, experimental tests could be performed to characterize the hysteretic behavior of the connections.

From the numerical analyses, it is possible to highlight the following results:

- The equivalent FEM is useful to define the roof design during the preliminary design phase;
- The analyses performed with the equivalent FEM represent a fast method to define the roof configuration that best achieves a global box behavior in seismic response;
- The performed analyses allow us to test different possible retrofitted roof configurations through various values of the hysteretic variable. On the contrary, during the conceptual design phase, the analysis of local mechanisms (also referred to as macro-elements) or the implementation of 3D models represent the standard approach to evaluate the capacity of the original construction;
- By performing nonlinear dynamic analyses, the EDR and the transversal drift of the roof are characterized by a similar variation as a function of the hysteretic variable $\beta_{\text{-}HYS}$;

- The TH approach gives EDR values lower than those evaluated by the PO analyses performed according to FEMA 356 and ATC-40;
- The effects of the SD and SSD hysteretic models are significant in terms of the dissipated energy during the seismic event;
- ATC-40 overestimates the EDR values, especially if the SD model is adopted;
- The optimal $\beta_{\text{-}HYS\text{-}opt}$ value detected in the transversal displacement diagram is also valid for the EDR estimation;
- For a hysteretic variable $\beta_{\text{-}HYS}$ greater than 1.5, the dissipative effect of the roof diaphragm no longer increases, indicating that the structural configuration becomes excessively rigid beyond this limit.

Author Contributions: Conceptualization, N.L., P.C., M.Z. and M.S.; methodology, N.L., P.C., M.Z. and M.S.; validation, N.L. and M.S.; formal analysis, N.L. and P.C.; investigation, N.L. and M.Z.; data curation, N.L. and M.S.; writing—original draft preparation, N.L. and P.C.; writing—review and editing, N.L., P.C., M.Z. and M.S.; visualization, M.Z. and N.L.; supervision, N.L. and P.C. All authors have read and agreed to the published version of the manuscript.

Funding: This research received no external funding.

Institutional Review Board Statement: Not applicable.

Informed Consent Statement: Not applicable.

Data Availability Statement: The original contributions presented in this study are included in the article. Further inquiries can be directed to the corresponding author.

Acknowledgments: The authors would like to thank to A. Franchi from Politecnico di Milano for the contribution to the successful completion of this study.

Conflicts of Interest: The authors declare no conflicts of interest.

References

1. Milani, G. Lesson Learned after the Emilia-Romagna, Italy, 20-29 May 2012 Earthquakes: A Limit Analysis Insight on Three Masonry Churches. *Eng. Fail. Anal.* **2013**, *34*, 761–778. [CrossRef]
2. Liberatore, D.; Doglioni, C.; AlShawa, O.; Atzori, S.; Sorrentino, L. Effects of Coseismic Ground Vertical Motion on Masonry Constructions Damage during the 2016 Amatrice-Norcia (Central Italy) Earthquakes. *Soil Dyn. Earthq. Eng.* **2019**, *120*. [CrossRef]
3. Longarini, N.; Crespi, P.; Zucca, M. The Influence of the Geometrical Features on the Seismic Response of Historical Churches Reinforced by Different Cross Lam Roof-Solutions. *Bull. Earthq. Eng.* **2022**, *20*, 6813–6852. [CrossRef]
4. Longarini, N.; Crespi, P.; Scamardo, M. Numerical Approaches for Cross-Laminated Timber Roof Structure Optimization in Seismic Retrofitting of a Historical Masonry Church. *Bull. Earthq. Eng.* **2020**, *18*, 487–512. [CrossRef]
5. Parisi, M.A.; Tardini, C. Seismic Vulnerability Assessment of Timber Roof Structures: Criteria and Procedures. *Proc. Inst. Civil. Eng. Struct. Build.* **2021**, *174*, 431–442. [CrossRef]
6. Giuriani, E.P.; Marini, A.; Preti, M. Thin-Folded Shell for the Renewal of Existing Wooden Roofs. *Int. J. Archit. Herit.* **2016**, *10*, 797–816. [CrossRef]
7. Department of Homeland Security. *FEMA 440: Improvement of Nonlinear Static Seismic Analysis Procedures*; Department of Homeland Security: Washington, DC, USA, 2005.
8. Castellazzi, G.; Gentilini, C.; Nobile, L. Seismic Vulnerability Assessment of a Historical Church: Limit Analysis and Nonlinear Finite Element Analysis. *Adv. Civil. Eng.* **2013**, *2013*, 517454. [CrossRef]
9. Micelli, F.; Cascardi, A. Structural Assessment and Seismic Analysis of a 14th Century Masonry Tower. *Eng. Fail. Anal.* **2020**, *107*, 104198. [CrossRef]
10. Shehu, R. Preliminary Assessment of the Seismic Vulnerability of Three Inclined Bell-Towers in Ferrara, Italy. *Int. J. Archit. Herit.* **2022**, *16*, 485–517. [CrossRef]
11. de Silva, F.; Ceroni, F.; Sica, S.; Silvestri, F. Non-Linear Analysis of the Carmine Bell Tower under Seismic Actions Accounting for Soil–Foundation–Structure Interaction. *Bull. Earthq. Eng.* **2018**, *16*, 2775–2808. [CrossRef]
12. Preciado, A. Seismic Vulnerability and Failure Modes Simulation of Ancient Masonry Towers by Validated Virtual Finite Element Models. *Eng. Fail. Anal.* **2015**, *57*, 72–87. [CrossRef]

13. Cannizzaro, F.; Pantò, B.; Lepidi, M.; Caddemi, S.; Caliò, I. Multi-Directional Seismic Assessment of Historical Masonry Buildings by Means of Macro-Element Modelling: Application to a Building Damaged during the L'Aquila Earthquake (Italy). *Buildings* **2017**, *7*, 106. [CrossRef]
14. Masciotta, M.G.; Lourenço, P.B. Seismic Analysis of Slender Monumental Structures: Current Strategies and Challenges. *Appl. Sci.* **2022**, *12*, 7340. [CrossRef]
15. Yu, L.L.; Dong, Z.Q.; Li, G. Simplified Mechanical Models for the Seismic Collapse Performance Prediction of Unreinforced Masonry Structures. *Eng. Struct.* **2022**, *258*, 114131. [CrossRef]
16. Xiang, M.; Shen, J.; Xu, Z.; Chen, J. Structure-to-structure Seismic Damage Correlation Model. *Earthq. Eng. Struct. Dyn.* **2024**, *53*, 3205–3229. [CrossRef]
17. Preti, M.; Loda, S.; Bolis, V.; Cominelli, S.; Marini, A.; Giuriani, E. Dissipative Roof Diaphragm for the Seismic Retrofit of Listed Masonry Churches. *J. Earthq. Eng.* **2019**, *23*, 1241–1261. [CrossRef]
18. Preti, M.; Bolis, V.; Marini, A.; Giuriani, E. Example of the Benefits of a Dissipative Roof Diaphragm in the Seismic Response of Masonry. In Proceedings of the SAHC2014–9th International Conference on Structural Analysis of Historical Constructions, Mexico City, Mexico, 4–17 October 2014.
19. Alvares da Silva, A.H.; Stojadinović, B. Surrogate Models for Seismic Response Analysis of Flexible Rocking Structures. *Earthq. Eng. Struct. Dyn.* **2024**, *53*, 3701–3725. [CrossRef]
20. Ceccotti, A.; Sandhaas, C.; Okabe, M.; Yasumura, M.; Minowa, C.; Kawai, N. SOFIE Project—3D Shaking Table Test on a Seven-Storey Full-Scale Cross-Laminated Timber Building. *Earthq. Eng. Struct. Dyn.* **2013**, *42*, 2003–2021. [CrossRef]
21. Valdivieso, D.; Almazán, J.L.; Lopez-Garcia, D.; Montaño, J.; Liel, A.B.; Guindos, P. System Effects in T-shaped Timber Shear Walls: Effects of Transverse Walls, Diaphragms, and Axial Loading. *Earthq. Eng. Struct. Dyn.* **2024**, *53*, 2532–2554. [CrossRef]
22. Johansen, K.W. *Theory of Timber Connections*; IABSE: International Association of Bridge and Structural Engineering: Zurich, Switzerland, 1949; Volume 9.
23. Shahnewaz, M.; Alam, S.; Tannert, T. In-Plane Strength and Stiffness of Cross-Laminated Timber Shear Walls. *Buildings* **2018**, *8*, 100. [CrossRef]
24. Sandhaas, C.; van de Kuilen, J.W.G. Strength and Stiffness of Timber Joints with Very High Strength Steel Dowels. *Eng. Struct.* **2017**, *131*, 394–404. [CrossRef]
25. Hossain, A.; Lakshman, R.; Tannert, T. Shear Connections with Self-Tapping Screws for Cross-Laminated Timber Panels. In Proceedings of the Structures Congress 2015, Portland, OR, USA, 23–25 April 2015.
26. *EN 1995-1-1*; Eurocode 5—Design of Timber Structures—General—Common Rules and Rules for Buildings. CEN: Brussels, Belgium, 2004; Volume 144.
27. Aloisio, A.; Alaggio, R.; Fragiacomo, M. Equivalent Viscous Damping of Cross-Laminated Timber Structural Archetypes. *J. Struct. Eng.* **2021**, *147*, 04021012. [CrossRef]
28. Barbosa, M.J.; Pauwels, P.; Ferreira, V.; Mateus, L. Towards Increased BIM Usage for Existing Building Interventions. *Struct. Surv.* **2016**, *34*, 168–190. [CrossRef]
29. Federal Emergency Management Agency. *Prestandard and Commentary for the Seismic Rehabilitation of Buildings*; FEMA 356; Federal Emergency Management Agency: Washington, DC, USA, 2000.
30. Applied Technology Council. *ATC 40, Seismic Evaluation and Retrofit of Concrete Buildings*; Seismic Safety Commission: West Sacramento, CA, USA, 1996; Volume 1.
31. Habieb, A.B.; Valente, M.; Milani, G. Base Seismic Isolation of a Historical Masonry Church Using Fiber Reinforced Elastomeric Isolators. *Soil Dyn. Earthq. Eng.* **2019**, *120*, 127–145. [CrossRef]
32. Valente, M.; Barbieri, G.; Biolzi, L. Seismic Assessment of Two Masonry Baroque Churches Damaged by the 2012 Emilia Earthquake. *Eng. Fail. Anal.* **2017**, *79*, 773–802. [CrossRef]
33. Valente, M.; Barbieri, G.; Biolzi, L. Damage Assessment of Three Medieval Churches after the 2012 Emilia Earthquake. *Bull. Earthq. Eng.* **2017**, *15*, 2939–2980. [CrossRef]
34. Cacciola, P.; Deodatis, G. A Method for Generating Fully Non-Stationary and Spectrum-Compatible Ground Motion Vector Processes. *Soil Dyn. Earthq. Eng.* **2011**, *31*, 351–360. [CrossRef]
35. Iervolino, I.; Galasso, C.; Cosenza, E. REXEL: Computer Aided Record Selection for Code-Based Seismic Structural Analysis. *Bull. Earthq. Eng.* **2010**, *8*, 339–362. [CrossRef]
36. Giuriani, E.; Marini, A. Wooden Roof Box Structure for the Anti-Seismic Strengthening of Historic Buildings. *Int. J. Archit. Herit.* **2008**, *2*, 226–246. [CrossRef]
37. Preti, M.; Bolis, V.; Giuriani, E.; Marini, A.; Peretti, M. *Studio Del Ruolo Del Diaframma Di Copertura Nel Comportamento Sismico Degli Archi Diaframma Nella Chiesa Parrocchiale Di Sirmione*; Technical Report n. 1; Università di Brescia: Brescia, Italy, 2013.
38. Genshu, T.; Yongfeng, Z. Seismic Force Modification Factors for Modified-Clough Hysteretic Model. *Eng. Struct.* **2007**, *29*, 3053–3070. [CrossRef]

39. Loss, C.; Hossain, A.; Tannert, T. Simple Cross-Laminated Timber Shear Connections with Spatially Arranged Screws. *Eng. Struct.* **2018**, *173*, 340–356. [CrossRef]
40. Iwan, W.D.; Gates, N.C. The Effective Period and Damping of a Class of Hysteretic Structures. *Earthq. Eng. Struct. Dyn.* **1979**, *7*, 199–211. [CrossRef]
41. Clough, R.W. *Effect of Stiffness Degradation on Earthquake Ductility Requirements*; UC Berkeley: Berkeley, CA, USA, 1966.
42. Otani, S. Hysteresis models of reinforced concrete for earthquake response analysis. *J. Fac. Eng. Univ. Tokyo Ser. B* **1981**, *36*, 125–159.
43. Takeda, T.; Sozen, M.A.; Nielsen, N.N. Reinforced Concrete Response to Simulated Earthquakes. *J. Struct. Div.* **1970**, *96*, 2557–2573. [CrossRef]
44. Jacobsen, L. Steady Forced Vibrations as Influenced by Damping. *Trans. Am. Soc. Mech. Eng.* **1930**, *52*, 169–181. [CrossRef]
45. Jacobsen, L. Damping in Composite Structures. In Proceedings of the 2nd World Conference on on Earthquake Engineering, Tokyo and Kyoto, Japan, 11–18 July 1960; Volume 2.
46. Jennings, P.C. Equivalent Viscous Damping for Yielding Structures. *J. Eng. Mech. Div.* **1968**, *94*, 103–116. [CrossRef]
47. Laguardia, R.; Franchin, P.; Tesfamariam, S. Risk-Based Optimization of Concentrically Braced Tall Timber Buildings: Derivative Free Optimization Algorithm. *Earthq. Eng. Struct. Dyn.* **2024**, *53*, 179–199. [CrossRef]
48. Priestley, M.J.N. *Myths and Fallacies in Earthquake Engineering, Revisited: The Ninth Mallet Milne Lecture*; IUSS Press: Pavia, Italy, 2003.
49. Chopra, A.K. *Dynamics of Structures*; Pearson Education: London, UK, 2019.
50. Elmenshawi, A.; Sorour, M.; Mufti, A.; Jaeger, L.G.; Shrive, N. Damping Mechanisms and Damping Ratios in Vibrating Unreinforced Stone Masonry. *Eng. Struct.* **2010**, *32*, 3269–3278. [CrossRef]
51. Lubliner, J.; Oliver, J.; Oller, S.; Oñate, E. A Plastic-Damage Model for Concrete. *Int. J. Solids Struct.* **1989**, *25*, 299–326. [CrossRef]
52. Lee, J.; Fenves, G.L. Plastic-Damage Model for Cyclic Loading of Concrete Structures. *J. Eng. Mech.* **1998**, *124*, 892–900. [CrossRef]
53. Valente, M.; Milani, G. Damage Assessment and Partial Failure Mechanisms Activation of Historical Masonry Churches under Seismic Actions: Three Case Studies in Mantua. *Eng. Fail. Anal.* **2018**, *92*, 495–519. [CrossRef]
54. Midas GEN 2023. Available online: https://support.midasuser.com/hc/en-us/articles/27773333780761--GEN-2023-v1-1-Release-Note (accessed on 30 January 2025).
55. Dong, H.; He, M.; Wang, X.; Christopoulos, C.; Li, Z.; Shu, Z. Development of a Uniaxial Hysteretic Model for Dowel-Type Timber Joints in OpenSees. *Constr. Build. Mater.* **2021**, *288*, 123112. [CrossRef]
56. Hong, J.-P.; Barrett, D. Three-Dimensional Finite-Element Modeling of Nailed Connections in Wood. *J. Struct. Eng.* **2010**, *136*, 715–722. [CrossRef]
57. He, M.; Lam, F.; Foschi, R.O. Modeling Three-Dimensional Timber Light-Frame Buildings. *J. Struct. Eng.* **2001**, *127*, 901–913. [CrossRef]
58. Totani, G.; Monaco, P.; Totani, F.; Lanzo, G.; Pagliaroli, A.; Amoroso, S.; Marchetti, D. Site Characterization and Seismic Response Analysis in the Area of Collemaggio, L'Aquila (Italy). In Proceedings of the 5th International Conference on Geotechnical and Geophysical Site Characterisation, ISC 2016, Gold Coast, Australia, 5–9 September 2016; Volume 2.
59. NTC2018, I.M. of I. Norme Tecniche per Le Costruzioni. DM 17/1/2018 (In Italian). *Gazzetta Ufficiale della Repubblica Italiana*. 2018. Available online: https://biblus.acca.it/download/norme-tecniche-per-le-costruzioni-2018-ntc-2018-pdf/ (accessed on 30 January 2025).